



ORIGINAL RESEARCH ARTICLE

Laser Butt Welding of 6.6mm-Thick D406A Ultra-High-Strength Steel: Part II—Bending Deformation Ability of Joints

Miaoxia Xie, Zongyang Lv, Jun Wu, Lixu Zhang, Han Yu, Jian Long, and Linjie Zhang

Submitted: 10 November 2023 / Revised: 11 July 2024 / Accepted: 17 July 2024

To address the insufficient bending deformation ability of laser-welded joints of D406A ultra-high-strength steel, the microstructures and mechanical performance of laser-welded joints (Joint-HT1 and Joint-HT2) of D406A steel prepared using two heat treatment (HT) processes were compared. One HT(heat treatment) process was combination of quenching and medium-temperature tempering, heated from the room temperature to 930 °C at 10 K/min, followed by 85 min of holding, oil quenching, heating to 300 °C in a furnace, holding for 180 min, and finally air-cooling to the room temperature (HT1), and the other was combination of high-temperature tempering, quenching, and medium-temperature tempering, heated at 10 K/min from the room temperature to 650 °C and held for 85 min, heated again to 930 °C and held for 68 min, oil-quenched, heated to 300 °C and held for 180 min, and air-cooled to the room temperature (HT2). The results show that the microstructures in the weld of Joint-HT1 mainly include tempered martensite, whereas the weld of Joint-HT2 not only contains tempered martensite but also martensite-austenite islands. Alteration of the microstructure gives rise to variations in the mechanical properties. The cross-sections of the two joints exhibited uniform microhardness, and the microhardness of the section of Joint-HT2 was approximately 140 HV lower than that of Joint-HT1 overall. Moreover, the front and back sides of Joint-HT2 were probably decarburized, whereas no decarburization was found on Joint-HT1. The average tensile strength and elongation of Joint-HT1 were 1746 MPa and 3.5%, respectively; those of Joint-HT2 were 1542 MPa and 7.2%, respectively. The average bending angles of Joint-HT1 and Joint-HT2 were separately 32.6° and 45°, respectively. The strength and bending angle of Joint-HT2 both satisfy the production requirements for pressure-resistant shells used in space shuttle.

Keywords bending performance, D406A ultra-high-strength steel, heat treatment, laser welding, microstructures in welds

1. Introduction

D406A ultra-high-strength steel, characterized by excellent strength and ductility, is an important structural material for manufacturing aerospace craft. In recent years, a reliable gas tungsten arc welding (GTAW) process and corresponding heat treatment (HT) processes have been developed for D406A ultra-high-strength steel, leading to wide application. Recently, the conventional GTAW method is found to incur large deformation in the welding process of new D406 steel structures, which causes poor product quality and a high rejection rate. In comparison, laser welding has advantages

such as high energy density, small heat zone, small welding-induced residual deformation, small distribution range of welding-induced residual tensile stress, and high welding efficiency, and it is easy to achieve automation. Therefore, it has been applied to weld ultra-high-strength steel in recent years (Ref 1-6).

Chen et al. compared the morphologies, microstructures, and mechanical performance of laser-welded joints of 3.5mm-thick D406A steel in four modes (lateral oscillation, vertical oscillation, circular oscillation, and no oscillation of laser beams). They found that the weld penetration was at maximum while the cross-sectional shape was asymmetric during the circular oscillation of the laser beams. Additionally, Hietala et al. succeeded in applying laser welding to weld lap joints of 6mm-thick low-alloyed ultra-high-strength steel, achieving full penetration (Ref 7). Chen et al. found that bubbles in the molten pool during the welding of D406A steel with a laser-GTAW hybrid heat source are impacted and burst into multiple small bubbles after encountering oscillating laser beams when the laser scanning speed was high. These small bubbles likely escape from the keyhole, thereby significantly reducing the porosity of the weld (Ref 8). Finally, Chen et al. obtained welded joints of 2.4mm-thick D406A steel with porosity of 0. Moreover, Chen et al. found that during the welding of 2mm-thick D406A steel with a laser-GTAW hybrid heat source, the continuous circular oscillation of light beams exerted a favorable stirring effect on the molten pool. This effect refines the equiaxed grains in the weld, increases the number of

Miaoxia Xie and Zongyang Lv, School of Mechanical and Electrical Engineering, Xi'an University of Architecture and Technology, Xi'an 710311, China; Jun Wu and Lixu Zhang, Xi'an Aerospace Power Machine Factory Co., Ltd., Academy of Aerospace Solid Propulsion Technology, Xi'an 710025, China; Han Yu, Jian Long, and Linjie Zhang, State Key Laboratory for Mechanical Behavior of Materials, Xi'an Jiaotong University, Xi'an 710049, China. Contact e-mails: xiemiaoxia@xauat.edu.cn and longjian@xjtu.edu.cn.

equiaxed grains, improves the plasticity of weld metals, and reduces the welding-induced residual stress by 40% (Ref 9). Wu et al. adopted a laser-GTAW hybrid heat source to study the processing properties of horizontal transverse welding of D406A steel (Ref 10). They discovered that laser oscillations led to a more even distribution of energy, enhanced the quality of fusion in the side walls, and prevented the formation of pore defects.

The research mentioned above focuses on materials with small thicknesses and provides methods for inhibiting pores, as well as improving the plasticity and ductility of welds in the processes of laser welding and welding with a laser-GTAW hybrid heat source. Ning et al. (Ref 11) proposed a design method for multi-layer multi-pass welding schemes for the narrow-gap laser wire-filling welding of D406A steel. Defect-free laser-welded joints of D406A steel with a thickness of 6.6 mm were obtained under the predicted optimal welding conditions, the production efficiency of which was approximately 3.75 times that of conventional GTAW welding. The tensile strength and elongation of the as-welded joints were higher than those of the GTAW joints, and the welding-induced residual deformation was only 21% of that during GTAW. In recent years, myriawatt high-power fiber laser technologies have been developed to provide more optional welding schemes for manufacturing metal structures. Taking advantage of the strong penetrability of high-power lasers, Michael Rethmeier et al. proposed an efficient laser welding method for low-alloyed high-strength steel with large heights of blunt edges and shallow grooves. First, full-penetration welding was adopted for laser welding of the butt region in the lower large blunt edge. Then, the upper groove was filled with a filler wire. Meanwhile, weld reinforcement is formed on the front side, creating a completely welded joint (Ref 12-14).

In fact, the poor plasticity and ductility of laser-welded joints of high-strength metals are a general problem (Ref 15). Particularly, the bending performance of joints of thick sheets during high-power laser welding is generally low and even unqualified. In general, post-weld HTs are regarded as an effective approach to eliminate non-uniformity of joints. Janicki studied disk laser welding of ARMOX 500 T armor steel with the thickness of 3.6 mm and reported the poor bending deformation ability of as-welded joints (Ref 16). Jena et al. and Guo et al. separately explored influences of the tempering temperature on the strength and microhardness of armor steel and quenched steel (Ref 17, 18). Wang et al. found that the strength and microhardness of direct quenched steel under 1500 MPa after tempering reduce due to expulsion of carbides from martensite, coarsening of laths, and reduction of disloca-

tion density (Ref 19). Luo et al. studied influences of local HTs of laser beams on bending performance of laser-welded joints of low-alloyed ultra-high-strength steel with the thickness of 3 mm (Ref 20). The findings indicate that the microhardness in areas subjected to local heat treatments is primarily influenced by the maximum temperature reached. Luo et al. further explored influences of local HTs of laser beams on front and back sides of welds on the front and back bending performance of joints. Results show that when the front and back bending angles both exceed 90°, the tensile strength of joints is about 1205 MPa (Ref 21).

The research systematically explored the microstructures and mechanical performance of laser wire-filling welded joints of D406A ultra-high-strength steel prepared using two HT processes, thus providing direct support for solving the low bending performance of joints of D406A ultra-high-strength steel. Meanwhile, the research is also of reference significance for controlling the performance of laser-welded joints of other high-strength steel or ultra-high-strength steel. The innovation presented in this paper lies in the achievement of a strong and durable plastic match for D406A ultra-high-strength steel laser wire filler welding joints through a modified heat treatment process.

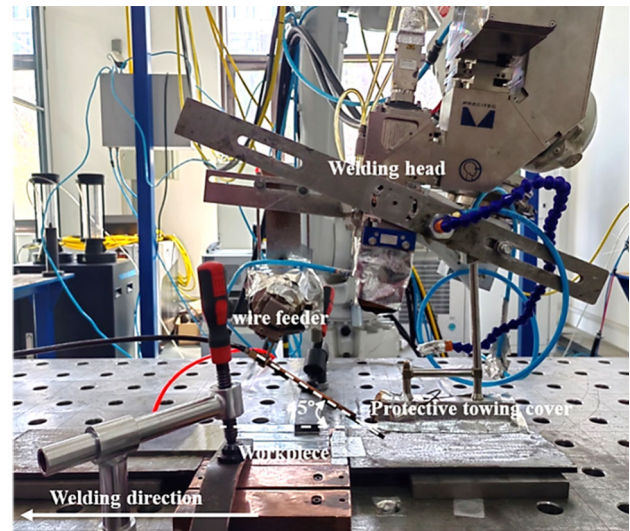


Fig. 1 The test platform for narrow-gap laser oscillating wire-filling welding

Table 1 Chemical compositions of D406A steel and H10 welding wire (wt.%)

	C	Si	Mn	Cr	Ni	Mo	V	Fe
D406A steel	0.27-0.32	1.40-1.70	0.70-1.00	1.00-1.30	0.25	0.40-0.55	0.08-0.15	Bal.
Welding wire	0.08-0.12	1.1-1.3	0.9-1.1	1.4-1.6	1.8-2.0	0.4-0.6	0.05-0.15	Bal.

2. Materials and Methods

2.1 Materials

The experimental material was annealed D406A ultra-high-strength steel with the thickness of 6.6 mm, of which the compositions are displayed in Table 1. H10 welding wire (H10SiMnCrNiMoV) with the diameter of 1.2 mm was used for welding, of which the chemical compositions are listed in Table 1. The material is provided by China Aerospace Science and Industry Corporation.

2.2 Methods

2.2.1 Experimental Equipment. As shown in Fig. 1, the laser welding equipment included an IPG YLS-8000 fiber laser, a Precitec YW52 oscillating laser welding head, an MXN-10 wire feeder, a MOTOMAN 6-axis robotic arm, a YASKAWA MOTOMAN-HP20D robot, a precision 3D sliding table, an argon shield, and a pressing plate. The laser used in the experiments had the maximum output power of 8 kW, wavelength of 1070 nm, focal length of 300 mm, and diameter of focal spot of 0.36 mm. The vertical motion range and the maximum transverse oscillation amplitude of the collimating lens of the YW52 oscillating laser welding head were separately ± 8 mm and 12 mm, and the maximum oscillation frequency could reach 500 Hz. In the welding process, the oscillating laser head was deviated by 5° from the vertical direction. The wire feed nozzle had an angle of 45° with the vertical direction, and the forward feed mode was employed. Figure 2 displays the top surface, back surface, and cross-section of the specimen plate. The width of the joint weld zone is 4.79 mm at the upper, 1.49 mm at the middle, and 2.83 mm at the bottom. The heat-affected zone measures approximately 0.91 mm at the upper, 0.79 mm at the middle, and 0.68 mm at the bottom.

2.2.2 Experimental Design. The groove shown in Fig. 3 was adopted, with the bottom width of 2 mm and height of the blunt edge of 5 mm. The aim of this paper is to weld structural parts with a wall thickness of 6.6 mm, so the plates thickness is 6.6 mm. Two D406A ultra-high-strength steel sheets with the groove were butted, and the scheme displayed in Fig. 4 was used for welding. The specific welding parameters are shown in

Table 2.

Two groups of different HT parameters were used after welding to perform HTs on the welded joints of D406A ultra-high-strength steel. The first was HT parameters currently used for laser joints of D406A steel: The samples were heated from the room temperature to 930°C at 10 K/min, followed by 85 min of holding, oil quenching, heating to 300°C in a furnace, holding for 180 min, and finally air-cooling to the room temperature (Fig. 5(a)). The second was a new HT process used for improving plasticity and ductility of weld metals: The samples were heated at 10 K/min from the room temperature to 650°C and held for 85 min, heated again to 930°C and held for 68 min, oil-quenched, heated to 300°C and held for 180 min, and air-cooled to the room temperature, as shown in Fig. 5(b).

2.2.3 Morphologies of Microstructures. The standard program was adopted to prepare cross-sectional metallographic samples of welded joints, the surface of which was corroded using nital of 4% for 10 s. Then, the corrodent was immediately washed away with clean water, and the samples were washed with ethyl alcohol. A Nikon MA200 optical microscope and a Hitachi SU8230 cold field emission scanning electron microscope (SEM) were utilized to observe cross-sectional morphologies and microstructures of welded joints. The SEM and Oxford HKL-Channel5 data collection software were adopted for electron backscattered diffraction (EBSD) observation and

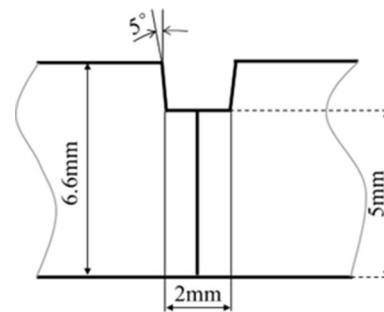


Fig. 3 Schematic diagram for the size of a narrow-gap groove on D406A steel of 6.6 mm thick

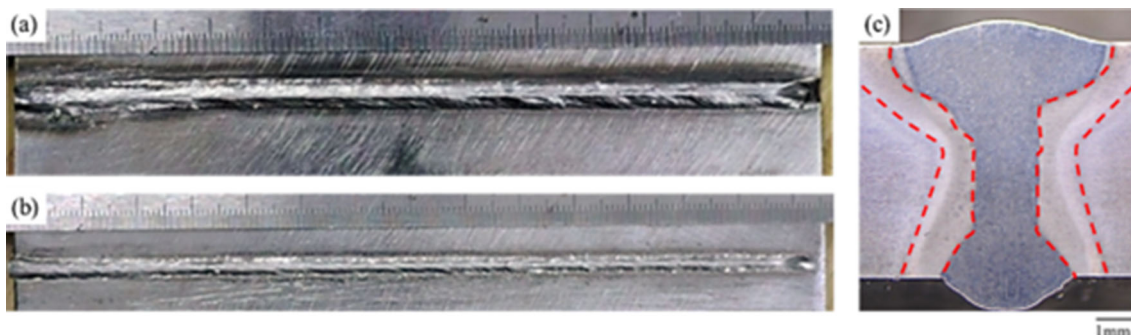


Fig. 2 Welded plate macrograph. (a) Upper surface morphology. (b) Back morphology. (c) Cross-sectional morphology

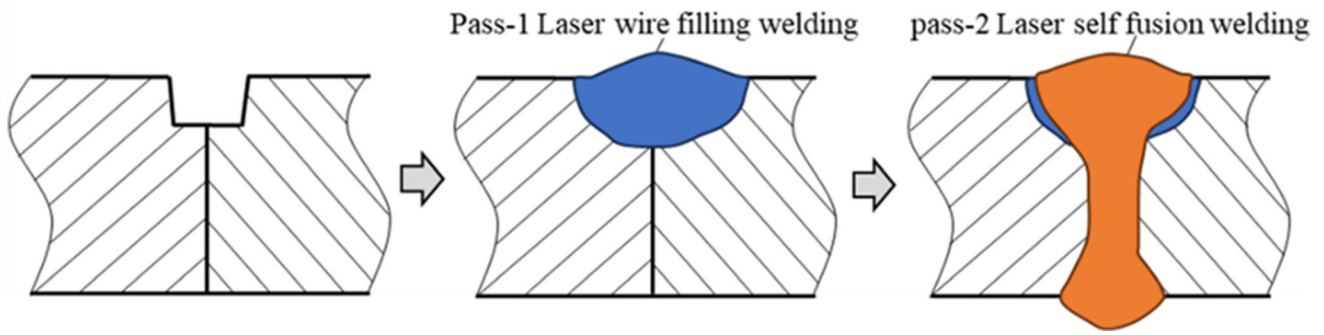


Fig. 4 Schematic diagram for welding process flows

Table 2 Welding parameters

	Laser power, W	Defocusing amount, mm	Welding speed, m/min	Wire feeding speed, cm/min	Oscillating frequency, Hz	Oscillating amplitude, mm	Heat input, kW/cm ²
Pass-1	4000	+ 28	0.48	290	150	0.4	3184.7
Pass-2	8000	0	0.96	/	70	0.8	6369.4

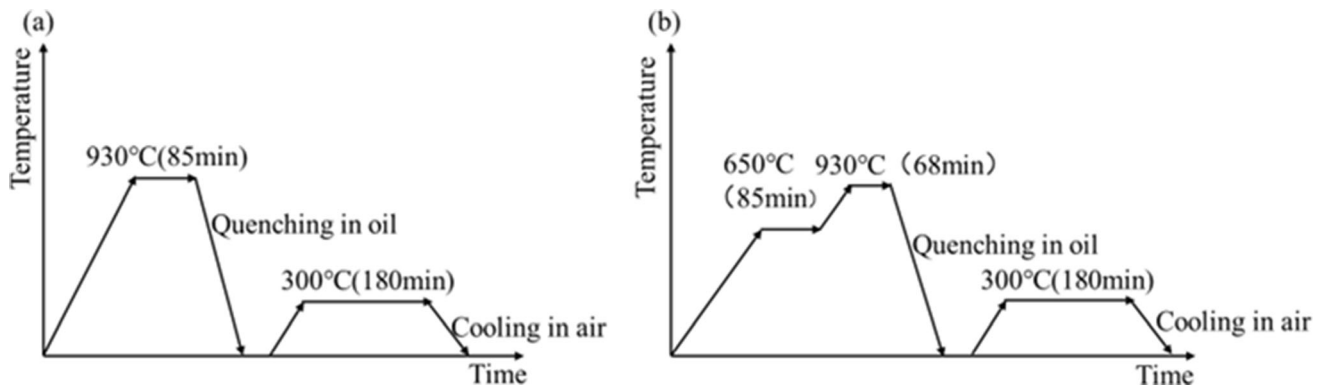


Fig. 5 Diagrams for two HT processes. (a) HT1. (b) HT2

data analysis experiments at the step of 0.2 μm . A JEM-2100F high-resolution transmission electron microscope (TEM) was used to observe morphologies of microstructures.

2.2.4 Mechanical Tests. An HV-1000TPTA Vickers hardness tester was utilized to test the microhardness of cross-sections of joints under a 200g load for 15 s. Microhardness distribution on four paths was tested: Microhardness was tested along the weld center in the vertical direction and on the upper, middle, and lower paths in the horizontal direction.

Room-temperature tensile tests were carried out following GB/T228.1-2021, and sample size is shown in Fig. 6(a). In the tests, the tension rate was 2 mm/min. Room-temperature bending tests were performed according to GB/T232-2010 on samples with the size in Fig. 6(b), during which the compression rate was 2 mm/min and the front side of the weld was tensioned. Finally, the Hitachi SU8230 cold field emission SEM was adopted to observe micromorphologies of fractures.

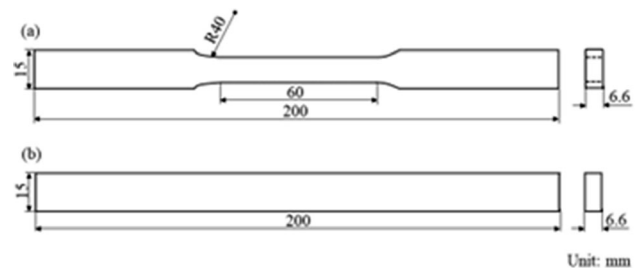


Fig. 6 Schematic diagram for sample sizes in mechanical tests (mm). (a) Tensile sample. (b) Bending sample

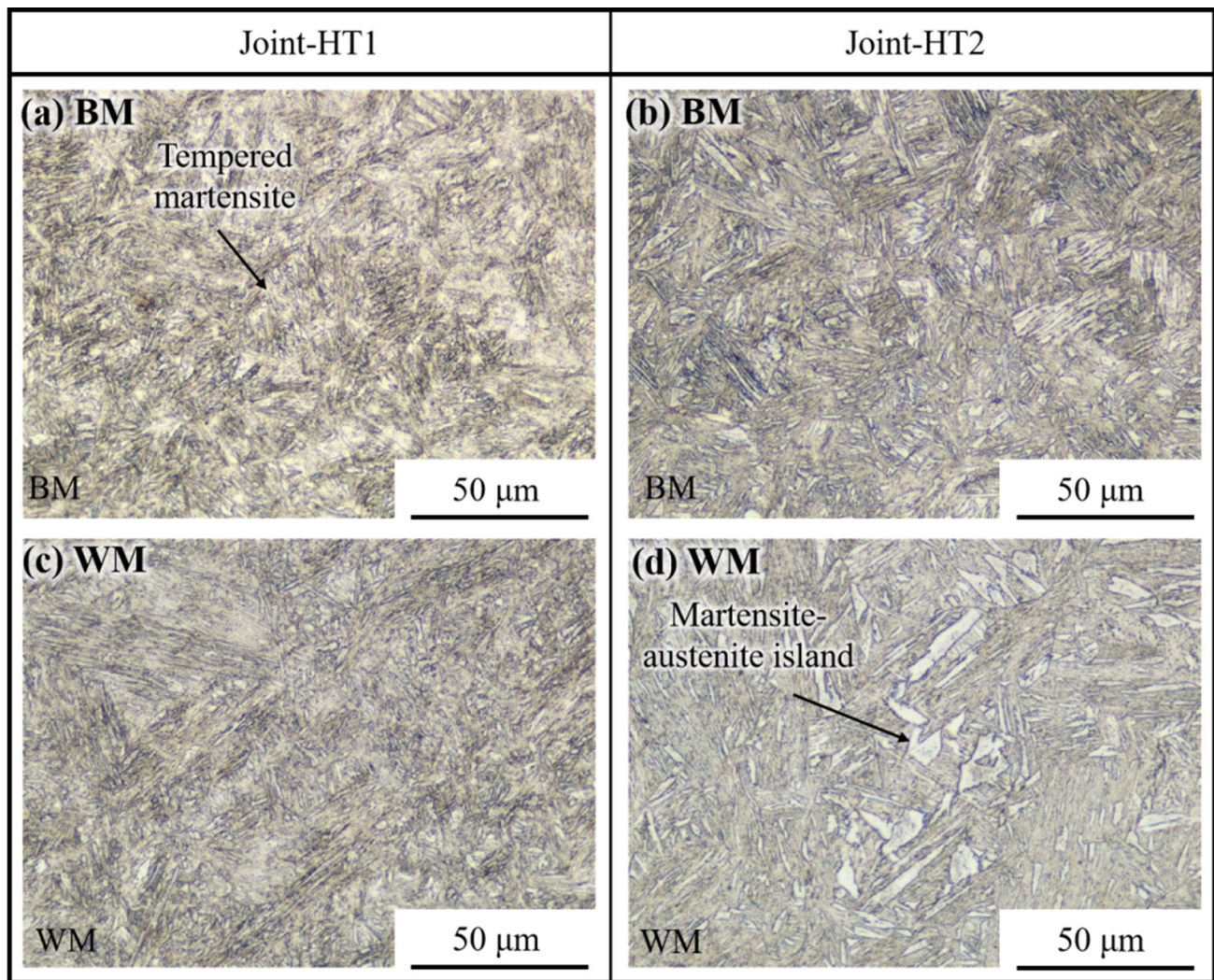


Fig. 7 Comparison of microstructures in the BM and FZ of welded joints under two HT systems

3. Results and Discussion

3.1 Morphologies of Microstructures

3.1.1 Microstructures in the Joints Under the Optical Microscope. Figure 7 compares the microstructures in the BM and FZ of the laser wire-filled welded joints of D406A steel under the two HT systems. The microstructures of the FZs of the two HT systems clearly differed. Figure 7(a) shows the microstructures in the BM under HT1, which are primarily composed of tempered martensite. Figure 7(b) shows microstructures in the BM under HT2, which are also mainly composed of tempered martensite. The difference is that the lath martensite in Fig. 7(b) is larger than in Fig. 7(a). Figure 7(c) shows the microstructures in the weld under HT1, which are similar to those in Fig. 6(a) and mainly consist of tempered

martensite. This is because the austenitizing temperature (AC_3) of D406A ultra-high-strength steel is 800 °C. The two HT processes in the research both involve quenching and low-temperature tempering, during which the quenching temperature is 930 °C, exceeding the austenitizing temperature of the material. When quenched at this temperature, the microstructures in each zone of the joints transformed into martensite. Then, the joints are subjected to low-temperature tempering at 300 °C, which is lower than the martensitic transformation temperature, so tempered martensite forms in the BM and FZ. The microstructures of weld of the joint obtained under HT2 are shown in Fig. 7(d). It is worth noting that compared with Fig. 7(c), this region contains not only tempered martensite but also martensite-austenite islands. This is probably because the holding time at 930 °C under HT1 is 85 min, while that at 930 °C under HT2 is 65 min. The quenching temperature for HT2 was the same as that for HT1, whereas the holding time

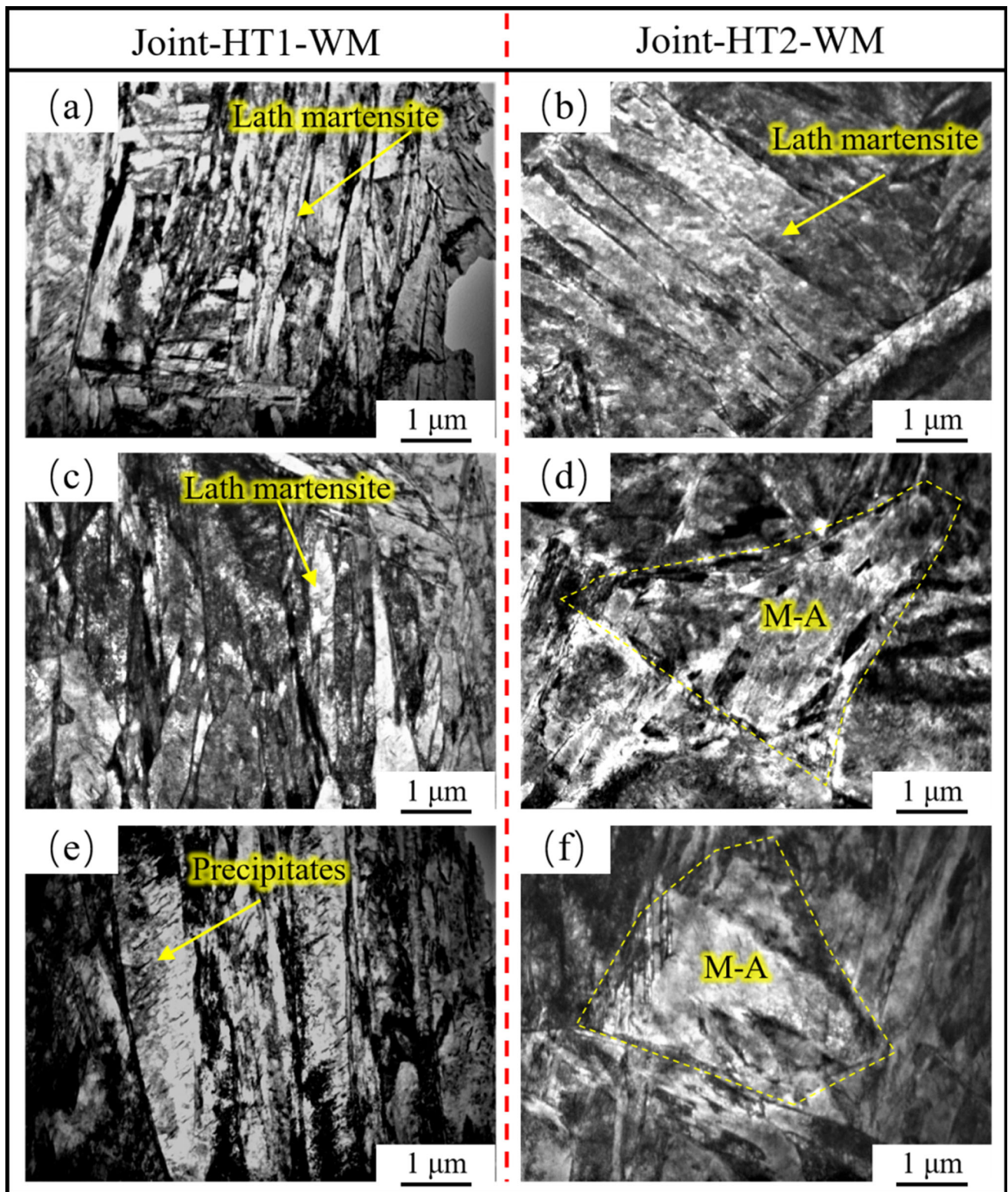


Fig. 8 Comparison of microstructures in joint weld areas under two HT systems under the TEM

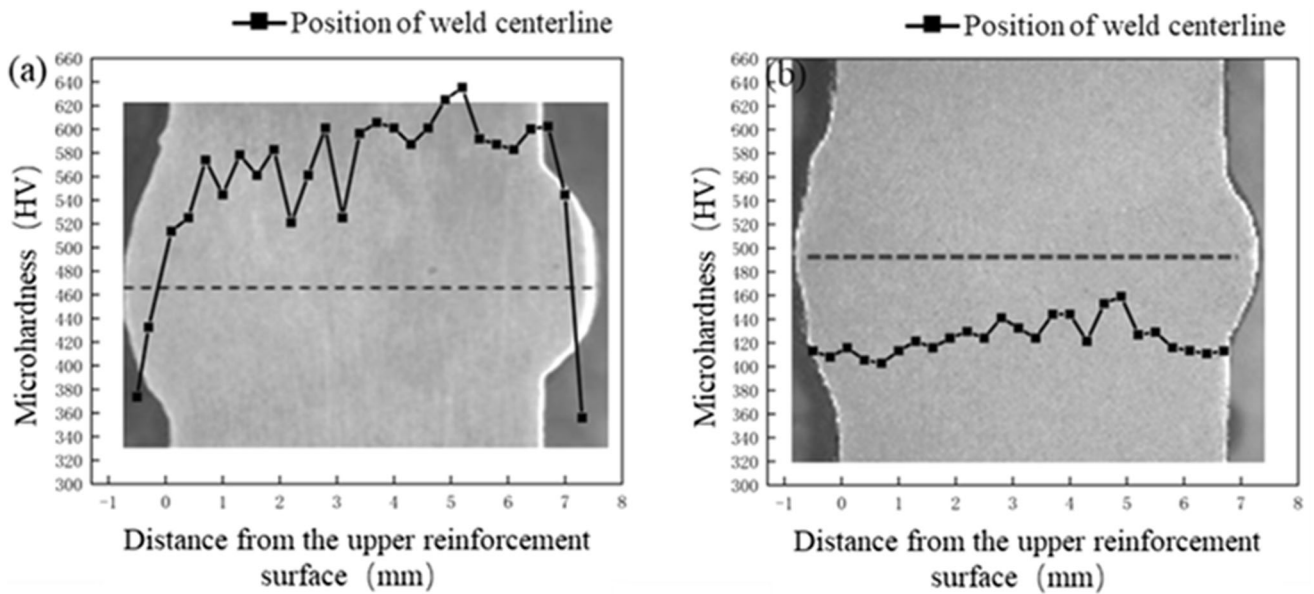


Fig. 9 Microhardness distribution in the weld center areas on the cross-sections of two quenched and tempered welded joints. (a) Joint-HT1. (b) Joint-HT2

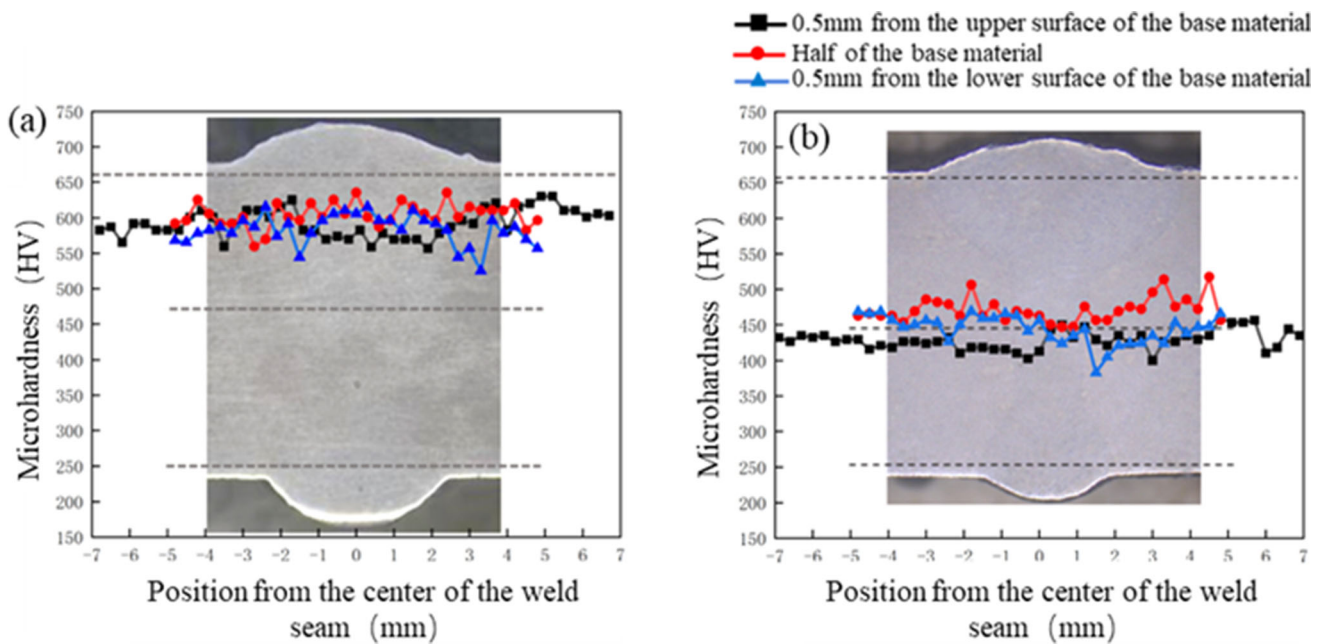


Fig. 10 Horizontal microhardness distribution on the cross-sections of two quenched and tempered welded joints. (a) Joint-HT1. (b) Joint-HT2

for HT2 was shorter than for HT1. Therefore, undercooled austenite probably does not have sufficient time to transform entirely into martensite under HT2, and some are retained to form a two-phase mixture, that is, martensite-austenite islands. It has been reported that increasing the number of martensite-austenite islands in steel may reduce its strength. It is notable that for martensite-austenite islands with sharp corners, due to proneness to stress concentration and cracks at the sharp

corners, the strength of the material decreases (Ref 22). The martensite-austenite islands shown in Fig. 7(d) are those with sharp corners.

3.1.2 Microstructures in Welds of Joints Under the TEM. Figure 8 compares the microstructures in the FZ of the joints in the two HT systems, as observed using TEM. Under TEM, the microstructures of the FZs differed for the two HT systems. Figure 8(a) and (c) shows the microstructures in the welds under HT1, which were mainly composed of a large

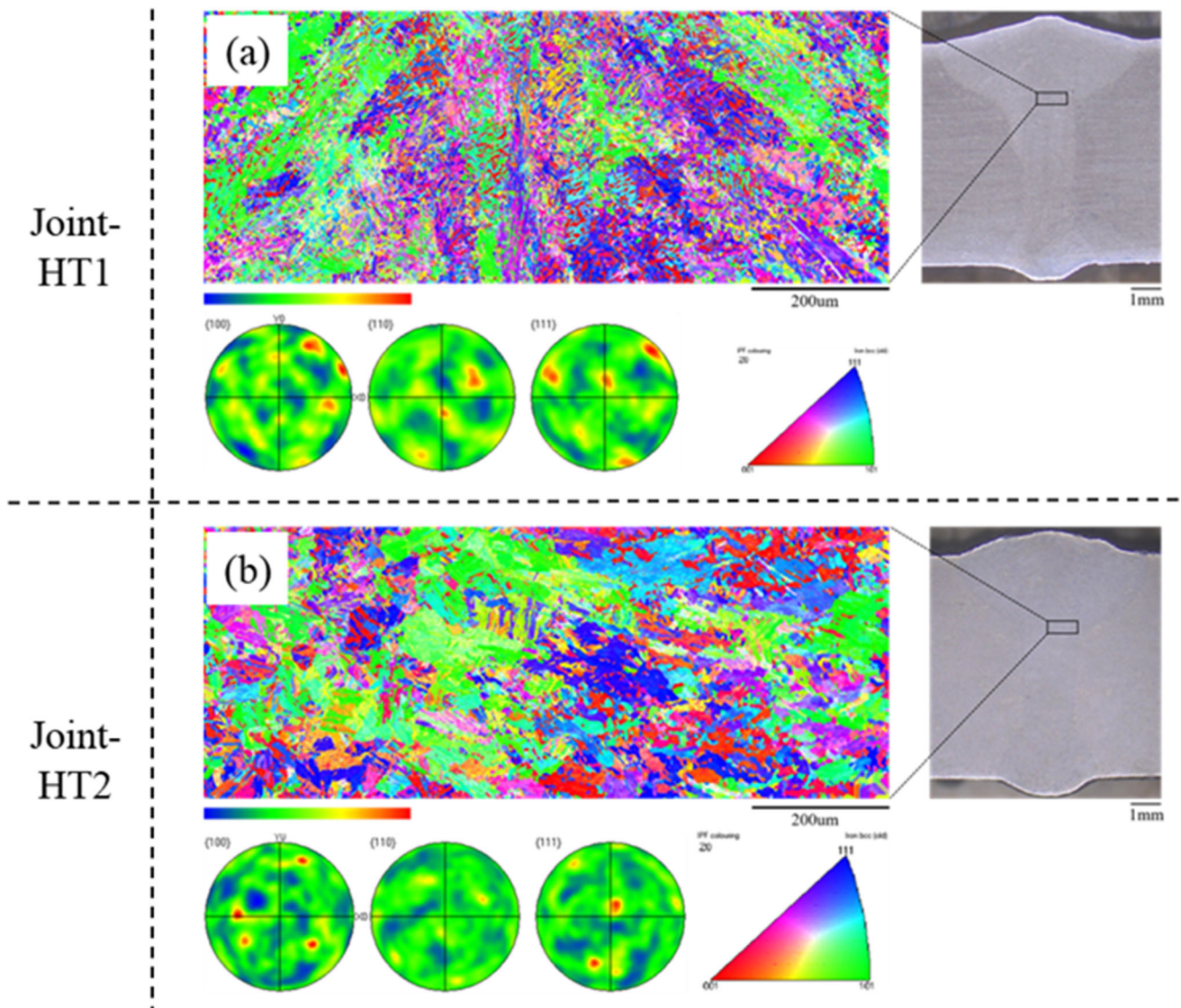


Fig. 11 Texture strength in the FZ of (a) Joint-HT1 and (b) Joint-HT2

amount of small lath martensite with a lath width of approximately 190 nm. Figure 8(b) shows the microstructures of the weld under HT2, which mainly include lath martensite. Compared with Fig. 8(a), the lath martensite in Fig. 8(b) is wider (approximately 620 nm). Some research has shown that, according to the Hall–Petch relation, the larger the lath martensite, the fewer the lath boundaries and the lower the resistance to dislocation motion during deformation, thus reducing the strength and microhardness of the materials (Ref 23). Compared with HT1, the growing width of the lath martensite under HT2 is an essential cause of the microhardness reduction in the FZ of the joint. Figure 8(d) and (f) displays the microstructures in the weld under HT2, in which martensite-austenite islands were observed. Figure 8(e) shows

the microstructures of the weld under HT1. A small portion of the lath martensite is widened in the FZ of the joint under HT1, whereas fine precipitates appear therein, dispersed in the lath martensite as fine needles. These fine particles hinder dislocation motion in steel and can effectively improve its strength and microhardness of steel (Ref 24). This is one of the important causes of the high microhardness in the FZ of Joint-HT1.

3.2 Microhardness

Figure 9 illustrates the microhardness distribution within the central regions of the welds, as observed in the cross-sections of the two quenched and tempered welded joints. Comparison of test results on Joint-HT1 and Joint-HT2 in Fig. 9 shows that the microhardness in the weld center area of Joint-HT2 (440 HV on

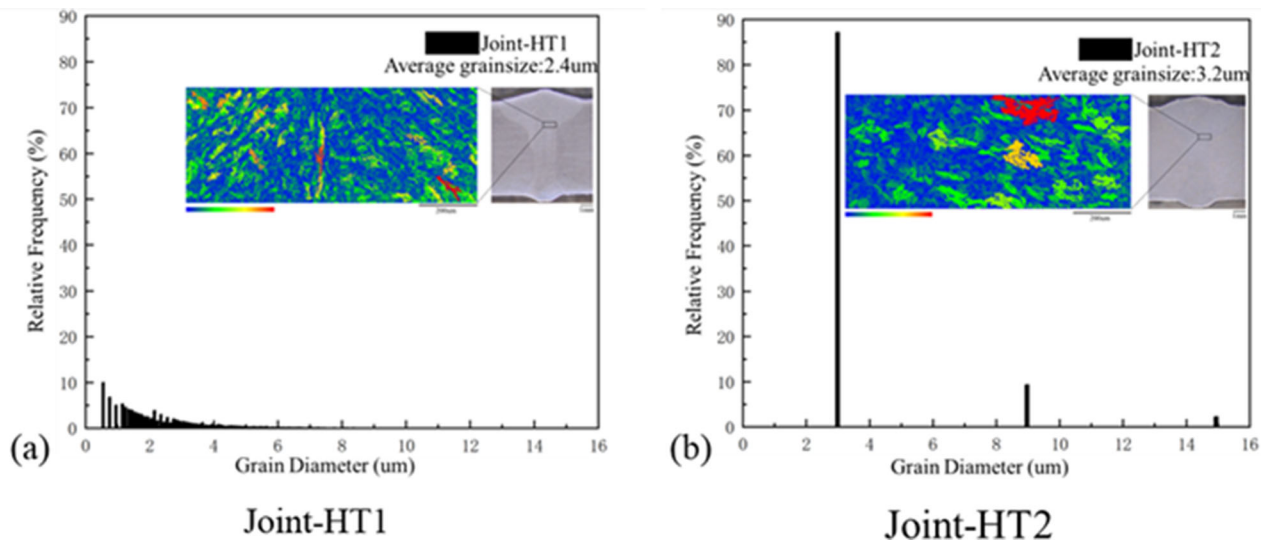


Fig. 12 Grain size in the FZ of (a) Joint-HT1 and (b) Joint-HT2

average) is noticeably lower than that of Joint-HT1 (540 HV on average). Moreover, the microhardness is distributed non-uniformly in the weld center area of Joint-HT1 along the thickness direction, whereas it shows a uniform distribution in Joint-HT2. In Fig. 9(a), the microhardness decreases in the weld center area of Joint-HT1 near the front and back sides. This was inferred to be the result of decarburization in areas near the surface. According to the curve in Fig. 9(a), the depth of the decarburized layer was approximately 0.5 mm. The curve in Fig. 9(b) indicates that Joint-HT2 was not decarburized, probably due to the short duration above the austenitizing temperature in the HT process of Joint-HT2, as shown in Fig. 4.

Figure 10(a) and (b) shows the horizontal microhardness distribution on cross-sections of Joint-HT1 and Joint-HT2. It can be seen from the microhardness distribution in the weld center areas of the two quenched and tempered welded joints that after HTs, microhardness exhibits uniform distribution on cross-sections of the two joints along the horizontal direction. Microhardness in Fig. 9(a) and (b) generally changes in ranges of 540-640 HV and 400-500 HV, that is, the microhardness of the weld of Joint-HT2 was lower than that of Joint-HT1. This is precisely what is expected in this research, i.e., improving the plasticity and ductility of joints by sacrificing strength.

3.3 Texture Strength, Grain Size, and Local Orientation Differences in Welded Joints

Figure 11 shows the texture strength results for the upper part of the weld fusion zone of the D406A laser-welded butt joint under the two heat treatment processes. Figure 11(a) shows the texture strength of the upper part of the HT1 fusion zone, where the maximum texture strength was 2.26. Figure 11(b) shows the texture strength of the upper part of the Joint-HT2 fusion zone, where the maximum texture strength was 2.69. The maximum texture strength varied slightly,

depending on the situation. Joint-HT2 outperformed Joint-HT1 in terms of texture strength, phase transition driving force, concentrated orientation, and equiaxed grains. This may result in uniform deformation when subjected to an external force, leading to an increase in the mechanical properties of the joint (Ref 25).

The grain sizes in the upper part of the weld fusion zone of the D406A laser-welded butt joint under the two heat treatment processes are compared in Fig. 12. Under the two heat treatment processes, there were significant differences in the average grain size of the weld fusion zone. The statistical results for the grain size at the top portion of the joint fusion zone of HT1 and HT2 are shown in Fig. 12(a) and (b), respectively. The average grain size of the two regions is 2.4 μm and 3.2 μm , respectively. The average grain size of the Joint-HT2 joint is small, the grain boundary area is large, and the hardness is low. As shown in Fig. 10(a), the microhardness of Joint-HT1 varied in the range of 540 HV-640 HV, and in Fig. 10(b), the microhardness of Joint-HT2 varied in the range of 400 HV-500 HV. The microhardness of Joint-HT2 was significantly lower than that of Joint-HT1. This is precisely the change expected in this study, i.e., by reducing the strength of the joint to improve its toughness.

Figure 13 shows the local orientation difference in the upper part of the weld fusion zone of the D406A laser-welded butt joint under the two heat treatment processes, which indirectly reflects the dislocation density and properties (Ref 26). As shown in Fig. 13, compared with the HT1 joint, the local orientation difference of the HT2 joint was lower, resulting in a smaller local dislocation density and improved joint toughness. As shown in Fig. 14, after the HT2 heat treatment system was adopted, the tensile strength of the laser-welded joint of D406A steel slightly decreased, and the elongation increased. The tensile strength of Joint II was 1546 MPa with an elongation of 7.5% and a bending angle of 49°. The mechanical properties of

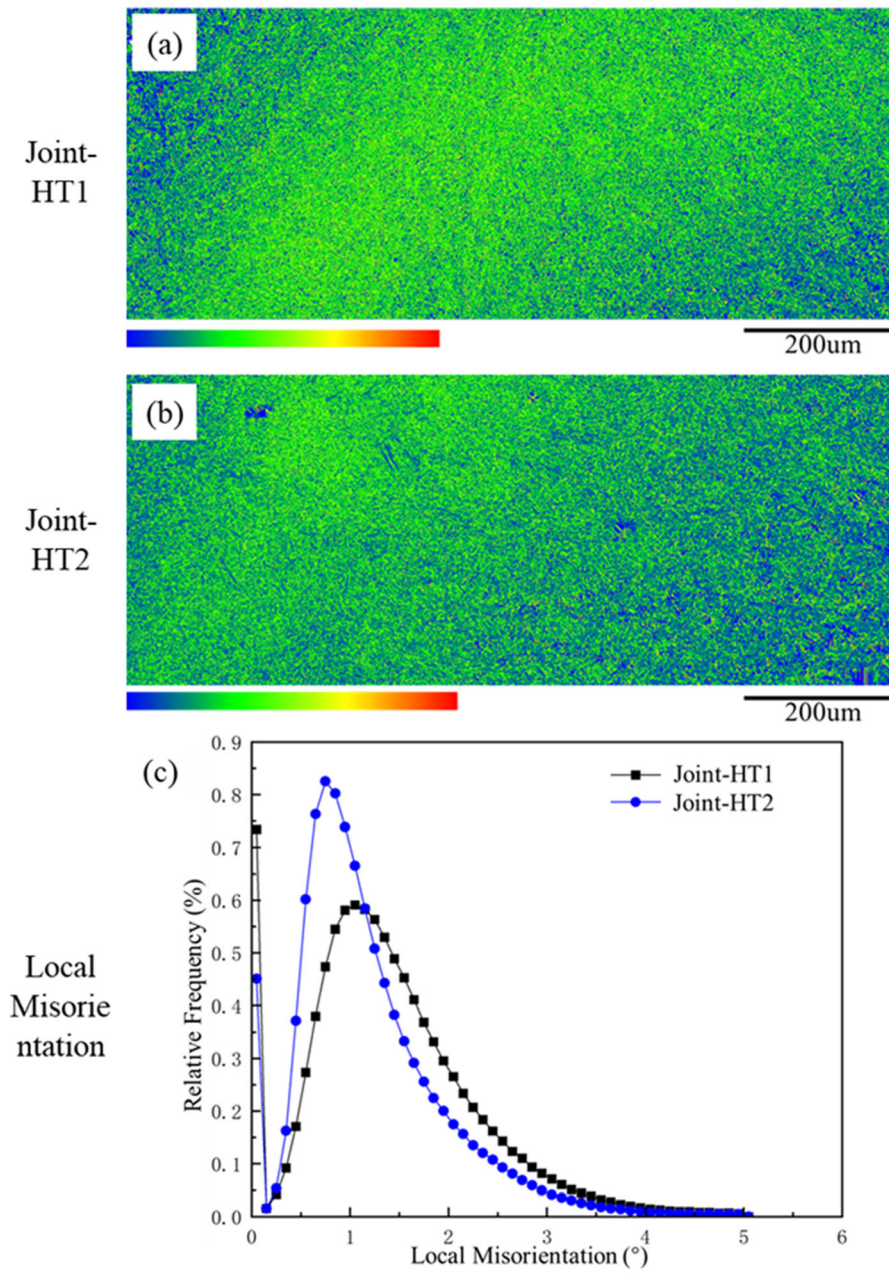


Fig. 13 Local orientation difference in the FZ of (a) Joint-HT1, (b) Joint-HT2, and (c) local misorientation

Joint-HT2 were improved to meet the industry requirements for strength and bending angle.

3.4 Tensile Test Results

Figure 14 displays the results of the room-temperature tensile tests of Joint-HT1 and Joint-HT2, and Table 3 lists the specific data. As shown in Fig. 14, the average tensile strength and elongation of Joint-HT1 are 1746 MPa and 3.5%, respectively, whereas those of Joint-HT2 are 1542 MPa and 7.2%, respectively. After adopting the new multi-stage HT, the

plasticity and ductility of the laser-welded joints of D406A improved significantly, whereas the tensile strength declined slightly. The figure also shows that Joint-HT1 and Joint-HT2 both fractured in the FZ during the tensile tests.

Figure 15 and 16 displays the SEM micromorphologies of the tensile fractures of Joint-HT1 and Joint-HT2. The fractures of Joint-HT1 and Joint-HT2 were found to be full of dimples, and both joints experienced ductile fractures in the FZs during tension. Compared to the fracture morphologies of Joint-HT1 in Fig. 15, the dimples on the fractures of Joint-HT2 in Fig. 16 were larger. The morphologies of the fibrous regions in the

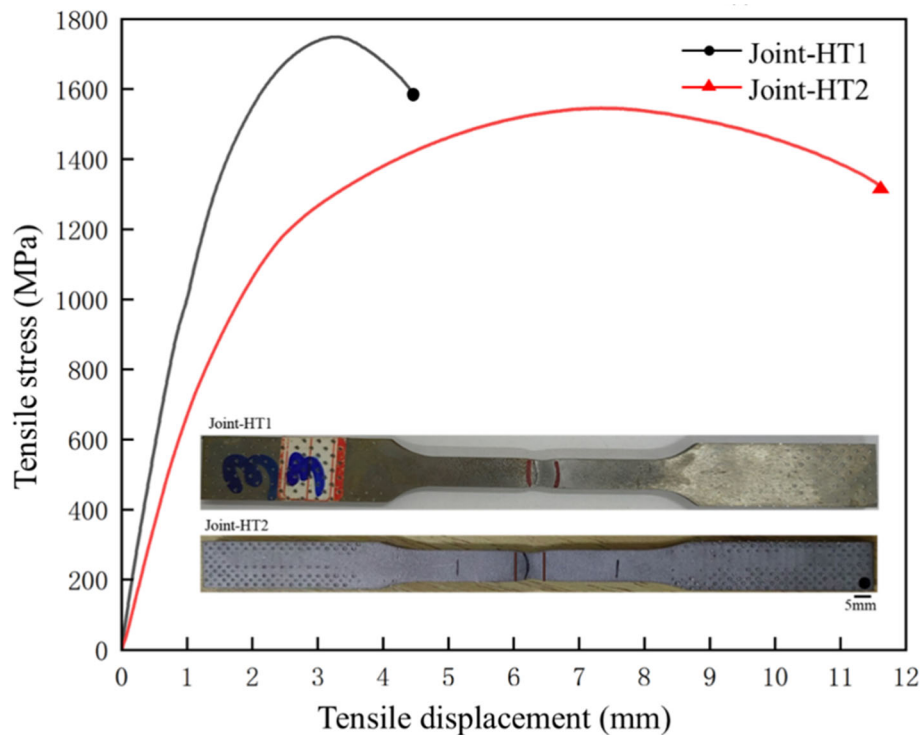


Fig. 14 Room-temperature tensile test results under two HT processes

Table 3 Room-temperature tensile test data under two HT processes

Joint	Average tensile strength, MPa	Average elongation, %
Joint-HT1	1746 ± 2.5	3.5 ± 0.6
Joint-HT2	1542 ± 5.0	7.2 ± 1.5

weld center areas and shear lips around the fractures can be clearly identified. This indicates that the plasticity of the weld metals was improved by utilizing the new multi-stage HT system (Ref 27).

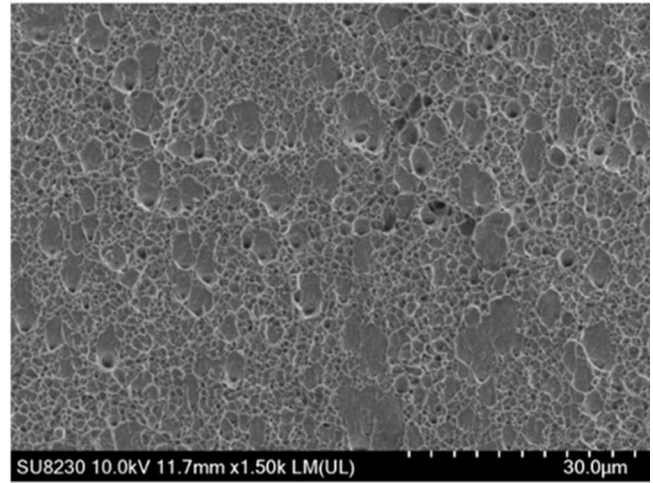
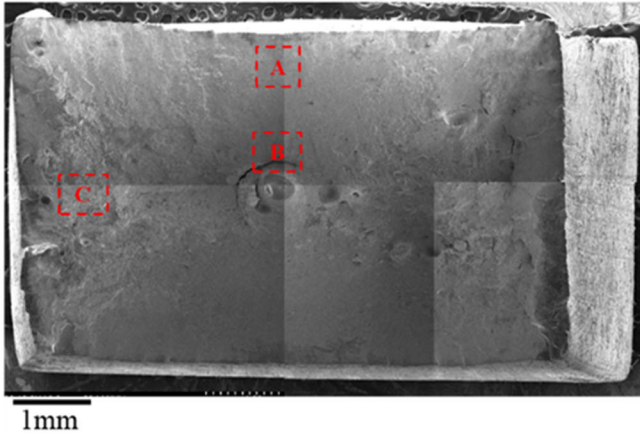
3.5 Bending Test Results

Figure 17 shows the three-point bending test results of Joint-HT1 and Joint-HT2 at room temperature. Specific data are presented in Table 4. As shown in Fig. 17(a), the average bending angles of Joint-HT1 and Joint-HT2 are 32.6° and 45°, separately. Figure 13(c) and 17(b) depicts the surface macro-morphologies in the side subjected to tensile stress of bending samples Joint-HT1 and Joint-HT2 after the bending tests. The industrial standard requires the bending angle of welded joints

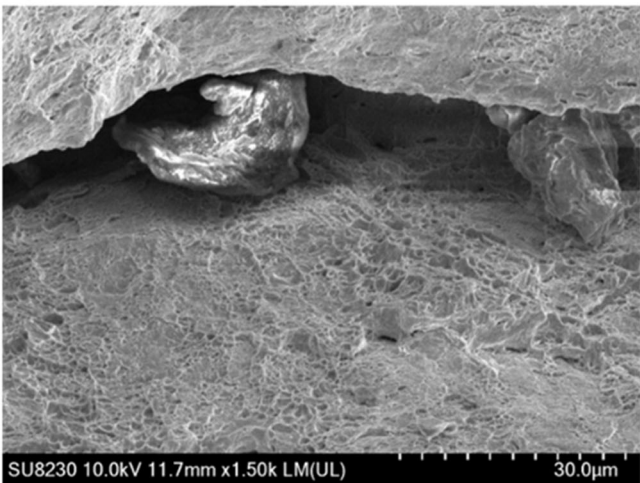
of D406A steel to be larger than 35°; therefore, the bending performance of Joint-HT2 meets technological requirements of the industry.

Compared with HT1, the increase in martensitic width is considered a factor contributing to the decrease in microhardness, as well as in improvement of toughness and bending properties in the FZ of the joint under HT2 conditions. Additionally, fine precipitates were present in some lath martensite within the FZ of the HT1 joint and were dispersed in a fine needle-like shape. These fine particles hinder dislocation movement within the steel, effectively improving its strength and microhardness. However, more was needed to improve the bending properties of the joints.

(a) SEM morphology of tensile fracture surface (b) Region A in (a)



(c) Region B in (a)



(d) Region C in (a)

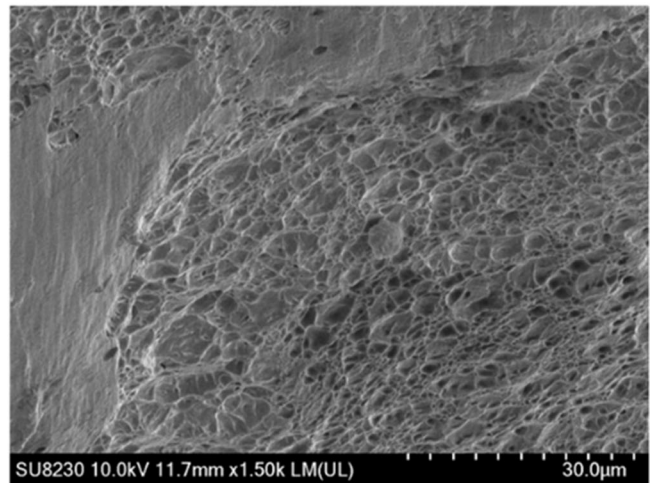


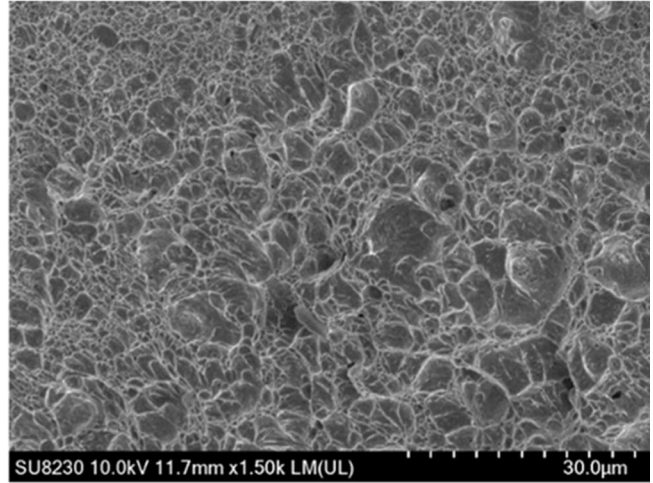
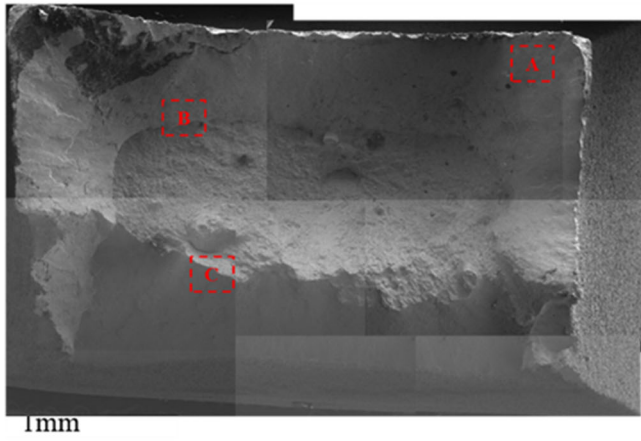
Fig. 15 SEM micromorphologies of tensile fracture surfaces of Joint-HT1

4. Conclusions

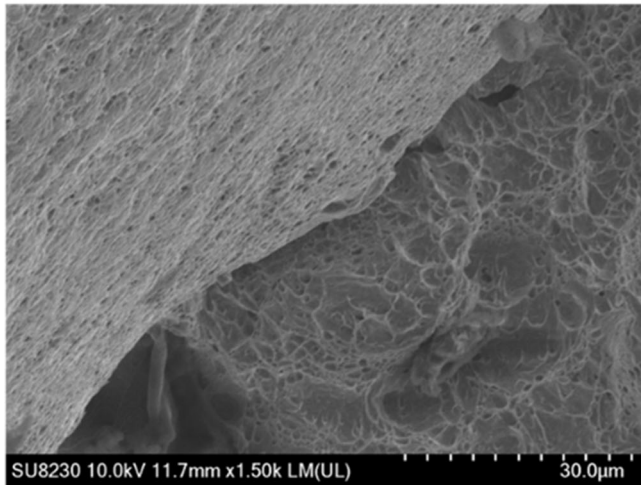
To solve the problems of high strength and insufficient bending deformation ability of laser-welded joints of D406A steel, laser-welded joints (Joint-HT1 and Joint-HT2) of D406A steel obtained using the two HT processes were compared in terms of their microstructures and mechanical performance. One of the HT processes was a combination of quenching and medium-temperature tempering (HT1), and the other was a combination of high-temperature tempering, quenching, and medium-temperature tempering (HT2). The following conclusions were drawn:

1. The microstructures in the weld of Joint-HT1 were mainly tempered martensite, while the FZ of Joint-HT2 contained not only tempered martensite but also martensite-austenite islands.
2. A small amount of lath martensite with significantly enlarged width was also observed in the FZ of Joint-HT1, and many fine needle-shaped precipitates are dispersed.
3. Microhardness was distributed uniformly on the cross-sections of the two joints. The microhardness of the cross-sections of Joint-HT1 and Joint-HT2 is in the ranges of 540-640 HV and 400-500 HV, respectively, meaning that the microhardness on the cross-section of Joint-HT2 was 140 HV lower than that of Joint-HT1.
4. After HT2, the plasticity and ductility of the laser-welded joints of D406A steel improved significantly, while the tensile strength decreased slightly. The bending angles of Joint-HT1 and Joint-HT2 were 32.6° and 45°, respectively. Both the strength and bending angle of Joint-HT2 satisfy industrial requirements.

(a) SEM morphology of tensile fracture surface (b) Region A in (a)



(c) Region B in (a)



(d) Region C in (a)

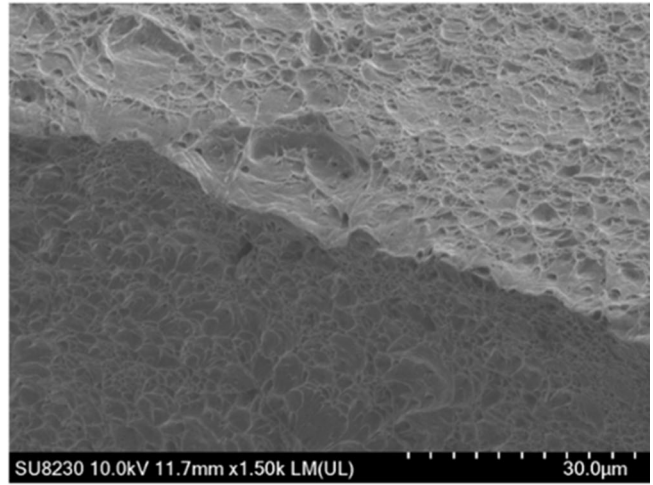


Fig. 16 SEM micromorphologies of tensile fracture surfaces of Joint-HT2



Fig. 17 Three-point bending test results of two quenched and tempered welded joints at room temperature

Table 4 Room-temperature bending test data under two HT processes

Joint	Bending angle (°)
Joint-HT1	32.6 ± 1.1
Joint-HT2	45.0 ± 3.3

Acknowledgments

This work was supported by the Natural Science Foundation of Shaanxi Province (Grant No. 2020JM-484).

Author contribution

Miaoxia Xie: Conceptualization, Data curation, Investigation, Writing - original draft, Writing - review & editing. Zongyang Lv: Investigation, Methodology, Writing - review & editing. Jun Wu: Investigation, Methodology, Funding acquisition. Lixu Zhang: Validation, Writing - review & editing, Supervision, Project administration, Resources. Han Yu: Investigation, Methodology, Writing - review & editing. Jian Long: Validation, Writing - review & editing. Linjie Zhang: Validation, Writing - review & editing.

Conflict of interest

The authors declare no conflict of interest.

Ethics approval

Not applicable.

Consent to participate

Not applicable.

Consent for publication

Not applicable.

References

- X. Zhang, Y. Chen, and J. Hu, Recent Advances in the Development of Aerospace Materials, *Prog. Aerosp. Sci.*, 2018, **97**, p 22–34
- Pan H. Development and Application of Lightweight High-Strength Metal Materials. In: MATEC Web of Conferences. EDP Sci 2018;207:03010
- G. Wang, Y. Yan, J. Li et al., Hydrogen Embrittlement Assessment of Ultra-High Strength Steel 30CrMnSiNi2, *Corros. Sci.*, 2013, **77**, p 273–280
- A. Kumar, and C. Pandey, Autogenous Laser-Welded Dissimilar Joint of Ferritic/Martensitic P92 Steel and Inconel 617 Alloy: Mechanism, Microstructure, and Mechanical Properties, *Arch. Civ. Mech. Eng.*, 2022, **22**, p 39
- G. Dak, S. Sirohi, and C. Pandey, Study on Microstructure and Mechanical Behavior Relationship for Laser-Welded Dissimilar Joint of P92 Martensitic and 304L Austenitic Steel, *Int. J. Press. Vessels Pip.*, 2022, **196**, 104629
- S. Sirohi, S.M. Pandey, V. Tiwari, D. Bhatt, D. Fydrych, and C. Pandey, Impact of Laser Beam Welding on Mechanical Behaviour of 2.25 Cr–1Mo (P22) Steel, *Int. J. Press. Vessels Pip.*, 2023, **201**, 104867
- M. Hietala, M. Ali, A. Khosravifard, M. Keskitalo, A. Järvenpää, and A. Hamada, Optimization of the Tensile-Shear Strength of Laser-Welded Lap Joints of Ultra-High Strength Abrasion Resistance Steel, *J. Mater. Res. Technol.*, 2021, **11**, p 1434–1442
- C. Chen, C. Wang, and N. Chen, Effect of Multiple Hit and Break of Oscillating Pulse Laser-TIG Hybrid Welding on Porosity Suppression of Ultra-High Strength Steel, *J. Manuf. Process.*, 2022, **83**, p 387–397
- C. Chen, W. Wang, and D. Li, Effect of Beam Oscillation on Microstructure and Properties of Laser-TIG Hybrid Welding of D406A Ultra-High Strength Steel, *J. Manuf. Process.*, 2020, **57**, p 798–805
- M. Wu, Z. Luo, Y. Li, L. Liu, and S. Ao, Effect of Heat Source Parameters on Weld Formation and Defects of Oscillating Laser-TIG Hybrid Welding in Horizontal Position, *J. Manuf. Process.*, 2022, **83**, p 512–521
- J. Ning, L.-J. Zhang, J.-N. Yang, X.-Q. Yin, X.-W. Wang, and J. Wu, Characteristics of Multi-pass Narrow-Gap Laser Welding of D406A Ultra-High Strength Steel, *J. Mater. Process. Technol.*, 2019, **270**, p 168–181
- M.O. Gebhardt, A. Gumenyuk, V.Q. Penaranda, and M. Rethmeier, Laser/GMA Hybrid Welding of Thick-Walled Precision Pipes, *Weld. Cut.*, 2012, **11**(5), p 312–318
- G. Turichin, M. Kuznetsov, A. Pozdnyakov, S. Gook, A. Gumenyuk, and M. Rethmeier, Influence of Heat Input and Preheating on the Cooling Rate, Microstructure and Mechanical Properties at the Hybrid Laser-Arc Welding of API 5L X80 Steel, *Procedia CIRP*, 2018, **74**, p 748–751
- S. Gook, A. Gumenyuk, and M. Rethmeier, Hybrid Laser Arc Welding of X80 and X120 Steel Grade, *Sci. Technol. Weld. Joining*, 2014, **19**(1), p 15–24
- A. Hamada, M. Ali, S. Ghosh, M. Jaskari, M. Keskitalo, and A. Järvenpää, Mechanical Performance and Formability of Laser-Welded Dissimilar Butt Joints Between Medium-Mn Stainless Steel and High-Strength Carbon Steel, *Mater. Sci. Eng. A*, 2022, **831**, 142200
- D. Janicki, Disk laser welding of armor steel, *Arch. Metall. Mater.*, 2014, **59**, p 1641–1646
- P.K. Jena, B. Mishra, M. Rameshbabu, A. Babu, A.K. Singh, K. SivaKumar, and T.B. Bhat, Effect of Heat Treatment on Mechanical and Ballistic Properties of a High Strength Armour Steel, *Int. J. Impact Eng*, 2010, **37**, p 242–249
- C. Guo, S. Long, H. Bo, and S. Zhang, Establishment of Tempering Characteristic Functions and Energy-Saving Heat-Treatment for Quenched Steels, *Heat Treat. Met.*, 2012, **37**, p 53–56
- L. Wang, Q. Cai, H. Wu, and W. Yu, Effects of Tempering Temperature on the Microstructure and Mechanical Properties of 1500 MPa Grade Steel Directly Quenched, *J. Univ. Sci. Technol. Beijing*, 2010, **32**, p 1150–1156
- C. Luo, Y. Zhao, Y. Cao, L. Zhao, and J. Shan, Effect of Laser Heat Treatment on Bending Property of Laser Welded Joints of Low-Alloy Ultra-High Strength Steel, *J. Laser Appl.*, 2019, **31**(3), p 032011
- C. Luo, Y. Cao, L. Zhao, and J. Shan, Laser Heat Treatment of Low-Alloy Ultrahigh-Strength Steel Laser-Welded Joints, *Weld. J.*, 2019, **98**(8), p 227S-240S
- H. Wang, Influences of Temperature-Holding Thickness and Finish Rolling Temperature on Martensite/Austenite Islands in X80 Pipeline Steel, *Mater. Mech. Eng.*, 2009, **33**, p 37–39
- Y. Liang, S. Long, Y. Lu, Y. Jiang, Y. Liang, and M. Yang, The Important Role of Martensite Laths to Fracture Toughness for the Ductile Fracture Controlled by the Strain in EA4T Axle Steel, *Mater. Sci. Eng. A*, 2017, **695**, p 154–164
- H. Sun, W. Lv, Y. Yang, D. Li, L. Yan, Y. He, and K. Gao, Optimizing the Hydrogen Embrittlement Resistance by Tuning the Structures of Cu-Rich Nanoprecipitates in High Strength Martensite Stainless Steels, *Acta Mater.*, 2023, **246**, p 118722
- R. Esterl, M. Sonnleitner, I. Weissensteiner, K. Hartl, and R. Schnitzer, Influence of Quenching Conditions on Texture and Mechanical Properties of Ultra-High-Strength Steels, *J. Mater. Sci.*, 2019, **54**, p 12875–12886
- M. Güden, H. Yavaş, A.A. Tanrikulu, A. Taşdemirci, B. Akin, S. Enser, A. Karakuş, and B.A. Hamat, Orientation Dependent Tensile Properties of a Selective-Laser-Melt 316L Stainless Steel, *Mater. Sci. Eng. A*, 2021, **824**, p 141808
- S. Sirohi, A. Gupta, C. Pandey, R.S. Vidyarthi, K. Guguloth, and H. Natu, Investigation of the Microstructure and Mechanical Properties of the Laser Welded Joint of P22 and P91 Steel, *Opt. Laser Technol.*, 2022, **147**, 107610

Publisher's Note Springer Nature remains neutral with regard to jurisdictional claims in published maps and institutional affiliations.

Springer Nature or its licensor (e.g. a society or other partner) holds exclusive rights to this article under a publishing agreement with the author(s) or other rightsholder(s); author self-archiving of the accepted manuscript version of this article is solely governed by the terms of such publishing agreement and applicable law.